Miniature curved artificial compound eyes

Dario Floreano[a,1], Ramon Pericet-Camara[a], Stéphane Viollet[b], Franck Ruffier[b], Andreas Brückner[c], Robert Leitel[c], Wolfgang Buss[c], Mohsine Menouni[d], Fabien Expert[b], Raphaël Juston[b], Michal Karol Dobrzynski[a], Geraud L'Eplattenier[a], Fabian Recktenwald[e], Hanspeter A. Mallot[e], and Nicolas Franceschini[b]

[a]Laboratory of Intelligent Systems, École Polytechnique Fédérale de Lausanne, CH-1015 Lausanne, Switzerland; [b]Aix-Marseille Université, Centre National de la Recherche Scientifique, Institut des Sciences du Mouvement, Unité Mixte de Recherche 7287, 13288 Marseille Cedex 09, France; [c]Fraunhofer Institute for Applied Optics and Precision Engineering, 07745 Jena, Germany; [d]Aix-Marseille Université, Centre National de la Recherche Scientifique, Centre de Physique des Particules de Marseille, Unité Mixte de Recherche 7346, 13288 Marseille Cedex 09, France; and [e]Laboratory of Cognitive Neuroscience, Department of Biology, University of Tübingen, 72076 Tübingen, Germany

Edited by Wilson S. Geisler, The University of Texas at Austin, Austin, TX, and approved April 23, 2013 (received for review November 7, 2012)

In most animal species, vision is mediated by compound eyes, which offer lower resolution than vertebrate single-lens eyes, but significantly larger fields of view with negligible distortion and spherical aberration, as well as high temporal resolution in a tiny package. Compound eyes are ideally suited for fast panoramic motion perception. Engineering a miniature artificial compound eye is challenging because it requires accurate alignment of photoreceptive and optical components on a curved surface. Here, we describe a unique design method for biomimetic compound eyes featuring a panoramic, undistorted field of view in a very thin package. The design consists of three planar layers of separately produced arrays, namely, a microlens array, a neuromorphic photodetector array, and a flexible printed circuit board that are stacked, cut, and curved to produce a mechanically flexible imager. Following this method, we have prototyped and characterized an artificial compound eye bearing a hemispherical field of view with embedded and programmable low-power signal processing, high temporal resolution, and local adaptation to illumination. The prototyped artificial compound eye possesses several characteristics similar to the eye of the fruit fly *Drosophila* and other arthropod species. This design method opens up additional vistas for a broad range of applications in which wide field motion detection is at a premium, such as collision-free navigation of terrestrial and aerospace vehicles, and for the experimental testing of insect vision theories.

bioinspired robotics | wide-angle vision | optic flow sensor | Micro-opto-electromechanical systems

Insect compound eyes consist of a mosaic of tiny optical units, or ommatidia (1). Compared with vertebrate single-lens eyes, compound eyes offer a versatile morphology with panoramic field of view (FOV), negligible distortion and aberration, and high temporal resolution, while trading high spatial resolution for diminutive size (2). These features are particularly beneficial for visually controlled navigation, including tasks like collision avoidance, take-off, landing, and other optomotor responses that do not require a high density of photoreceptors. Insect compound eyes possess local sensory adaptation mechanisms capable of compensating for large changes in light intensity right at the photoreceptor level (3, 4), and they wrap around highly distributed neuronal circuitry, allowing for fast and low-power integrated signal processing (5), whereas minimizing the overall size of the insect head. An artificial compound eye exhibiting all these properties would represent an ideal miniature sensor for numerous situations in which fast motion detection across wide FOVs is required (6–9).

Attempts have recently been made to develop miniature compound eyes. Both planar (10) and curved (11–14) microlens arrays have been fabricated. In some cases, these were interfaced with conventional flat CMOS arrays, but this resulted in off-axis aberrations, crosstalk between neighboring ommatidia, or limited FOV. At first sight, recent developments in flexible sensors (15–18) could represent a promising avenue for curved vision sensors (19, 20). However, adapting those flexible technologies to the design of curved compound eyes is challenging due to the recurring problem of precisely aligning a curved photodetector array with a curved microlens array. None of these previous methods or other available omnidirectional camera systems (21) display important features of biological compound eyes, such as embedded data processing, versatile morphologies, high temporal resolution, and local light adaptation in a miniature package.

Here, we describe a unique approach to the design of a curved artificial compound eye, named CurvACE. We validate this approach by characterizing the sensitivity, angular resolution, and motion extraction capabilities of a prototype bearing a semicylindrical morphology (Fig. 1*A*) and a hemispherical FOV of 180° × 60° (Fig. 1*B*). This prototype is a self-contained, integrated, curved artificial compound eye system with morphology and properties resembling those of primitive (22) (Fig. 1*C*) and modern (1) (Fig. 1*D*) arthropods. In particular, the CurvACE prototype features several similarities with the eye of the fruit fly *Drosophila*, namely, spatial resolution, acceptance angle, number of ommatidia, local light adaptation, crosstalk prevention, and signal acquisition bandwidth, as well as a smaller but comparable FOV (Table 1). Such curved visual sensors may be useful for terrestrial and aerial vehicles, medical instruments, prosthetic devices, home automation, surveillance, motion capture systems, and smart clothing. Artificial compound eyes may also foster the development of alternative visual algorithms, and when fitted on physical robots, they could help explore fundamental principles in animal sensory-motor control (6, 8, 9, 23).

Fabrication Process

Design Method. As with biological compound eyes, CurvACE artificial ommatidia consist of three materially and functionally different layers (Fig. 2*A*): (*i*) an optical layer composed of an array of highly transparent polymer microlenses molded on a glass carrier (Fig. S1), which focus light precisely onto (*ii*) the sensitive areas of a silicon-based photodetector layer. This layer contains an array of analog very-large-scale integration (VLSI) photodetectors as well as additional circuitry to condition the signal for processing (Fig. S2). Finally, (*iii*) a flexible electromechanical interconnection layer, formed by a polyimide printed circuit board (PCB), physically supports the ensemble and transfers the output signals from the individual ommatidia (Fig. 2*B*) to the processing units. With thicknesses of 550 μm, 300 μm, and 100 μm, respectively, the total

Author contributions: D.F., S.V., A.B., and N.F. designed research; R.P.-C., R.L., W.B., M.M., F.E., R.J., M.K.D., G.L., and F. Recktenwald performed research; S.V., F. Ruffier, R.L., W.B., M.M., F.E., R.J., G.L., and F. Recktenwald contributed with technical and analytic tools; D.F., R.P.-C., S.V., F. Ruffier, A.B., R.L., W.B., M.M., F.E., R.J., F. Recktenwald, H.A.M., and N.F. analyzed data; and D.F., R.P.-C., S.V., F. Ruffier, A.B., R.L., F. Recktenwald, H.A.M., and N.F. wrote the paper.

The authors declare no conflict of interest.

This article is a PNAS Direct Submission.

[1]To whom correspondence should be addressed. E-mail: dario.floreano@epfl.ch.

This article contains supporting information online at www.pnas.org/lookup/suppl/doi:10.1073/pnas.1219068110/-/DCSupplemental.

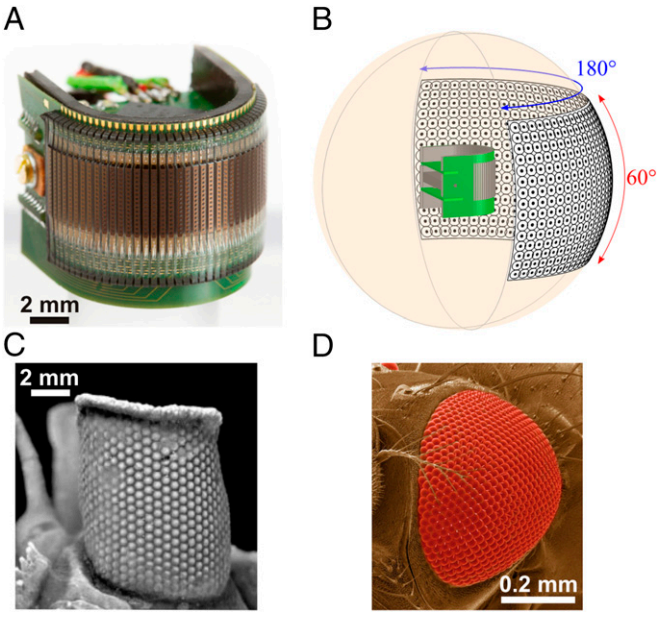

Fig. 1. Artificial and natural curved compound eyes. (*A*) Image of the CurvACE prototype. The entire device occupies a volume of 2.2 cm^3, weighs 1.75 g, and consumes 0.9 W at maximum power. (*B*) Illustration of the panoramic FOV of the fabricated prototype. The dots and circles represent the angular orientation and acceptance angle $\Delta\rho$ of every ommatidium, respectively. Compound eye of the extinct trilobite *Erbenochile erbeni* (22) (*C*) and of the fruit fly *Drosophila melanogaster* (*D*). [(*C*) Reprinted from ref. 22 with permission from AAAS; (*D*) Reprinted from ref. 44 with permission from AAAS.]

height of the three assembled layers is less than 1 mm in the prototype presented here.

The apposition and neural superposition compound eyes of many arthropod species contain pigmented sidewalls that contribute to reducing optical crosstalk between ommatidia (1). Our solution to suppress optical crosstalk makes use of two low-reflective opaque metal layers with matching pinhole patterns: one subjacent to the microlens array and the other one close to the focal plane, ahead of the photodetector layer (10) (Fig. 2 *A* and *B* and Fig. S1*C*).

The proposed design method is based on a planar fabrication technology for each of the three layers of the artificial ommatidia array, followed by high-precision cutting (dicing) of the rigid ommatidia layers to add bendability. Specifically, each of the three layers is fabricated at first with wafer-level (optical and photodetector layer) or batch-level (interconnection layer) processes using standard microengineering technologies (Figs. S1 and S2). Next, the optical and photodetector layers are aligned at micrometer accuracy and glued chip-wise (Fig. 2*B*). Subsequently, the ensemble is fixed and wire-bonded to the electromechanical interconnection layer. Finally, the rigid optical and photodetector layer stack is precisely separated with a chip dicing saw in columns of ommatidia down to the flexible interconnection layer, which remains intact (Fig. 2*C* and Fig. S3*A*). This procedure ensures accurate and reproducible alignment of the optical and photosensitive elements across the array while providing electronic accessibility to the output signals of the individual artificial ommatidia. It results in a very thin and light package, less than 1 mm and 0.36 g in the prototype presented here, and ensures mechanically safe bending of the interconnection layer down to a small radius of curvature (Fig. 2*D*). Free space on the backside of the artificial ommatidia permits attachment to curved rigid or flexible substrates and incorporation of additional electronics for signal processing in the resulting concavity (Fig. 2*D*).

Table 1. Specifications of CurvACE prototype compared with the characteristics of the *Drosophila melanogaster* compound eye

	CurvACE	*Drosophila* eye [Ref(s).]
Number of ommatidia	630	600–700
Facet diameter, μm	172	16 (42)
Eye diameter, mm	12.8	0.36 (42)
Facet diameter/eye diameter, %	1.3	4.4
Interommatidial angle, $\Delta\varphi$; deg.	~4.2	~4.7–5.5 (42)
Acceptance angle, $\Delta\rho$; deg.	4.2	~4.5 (24)
FOV, deg.	180 × 60	160 × 180 (43)
Signal acquisition bandwidth, Hz	300	<100 (28)
Adaptability to illuminance	Yes	Yes (4)
Crosstalk prevention	Yes	Yes (24)

deg., degree.

Fabrication of a CurvACE Prototype. We fabricated a CurvACE prototype by bending a rectangular array of 42 columns of 15 artificial ommatidia (microlens diameter = 172 μm) down to a curvature radius of 6.4 mm along its longer direction to yield a 180° FOV in the horizontal plane (Fig. 1 *A* and *B* and Fig. S3 *B* and *C*). This curvature should nominally yield an interommatidial angle $\Delta\varphi_h$ of 4.3° in the equatorial row along the bent direction. Although there is no mechanical bending along the vertical direction, it is possible to make the visual axes of the 15 ommatidia in each column fan out in the vertical plane by making the vertical pitch between the photodetectors stepwise smaller than the vertical pitch between the microlenses (10) (Fig. S1*C*). In the prototype, the photodetector pitch was calculated so as to obtain a similar value for the interommatidial angle $\Delta\varphi_v$ along the vertical unbent direction, which results in a total vertical FOV of 60° (Fig. 1*B*). To avoid spatial aliasing or blind spots in the visual field, the acceptance angle $\Delta\rho$ of each ommatidium must closely approach the interommatidial angle $\Delta\varphi$ (1, 24) (Fig. 3*C*). Therefore, the ommatidial lenslets, diaphragms, and photodetectors were designed using an optical ray tracing technique (Zemax; Radiant Zemax, LLC) to produce an acceptance angle $\Delta\rho$ of 4.3°.

The resulting concavity on the backside of the prototype after the mechanical bending along the horizontal direction is used to host two microcontrollers, two inertial sensors, and other electronic components that are fitted and soldered on two rigid PCBs (Fig. 2*D* and Figs. S3*C* and S4). In the experiments described below, the embedded microcontrollers are programmed to operate the visual data read-out and communicate with an external computer for analysis; in a stand-alone application, these microcontrollers can be used to process visual data onboard the prototype without any external computer.

Results

Characterization of Visual Sampling. To characterize the visual sampling of the environment by the fabricated CurvACE prototype, we measured the angular sensitivity function (ASF) of each of the 630 artificial ommatidia (Fig. S5). Fig. 3 *A* and *D* shows representative examples of ASFs measured along a single row and a single column, respectively. Most ASFs display the expected Gaussian distribution with respect to the light incidence angle, which validates both the microoptical design and the precise alignment with each individual photodetector. We derived the experimental acceptance angles and interommatidial angles from the measured ASFs. The acceptance angle $\Delta\rho$ of an ommatidium is defined as the full width at half maximum (FWHM) of its Gaussian-like ASF. The horizontal and vertical interommatidial angles $\Delta\varphi_h$ and $\Delta\varphi_v$ were assessed from the angular position of the peak of the ASFs of two adjacent ommatidia (Fig. 3*C*). The measured acceptance angles yielded an average of $\Delta\rho$ of 4.2° ± 0.3° (SD) for both

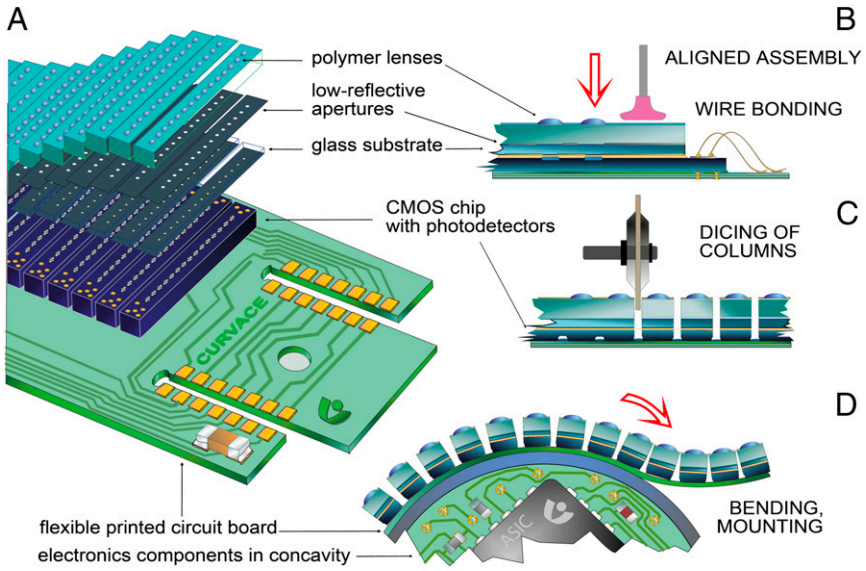

Fig. 2. CurvACE design and assembly. (*A*) Scheme of the three layers that compose the CurvACE artificial ommatidia: optical (microlenses and apertures), photodetector (CMOS chip), and interconnection (PCB). (*B*) Accurate alignment and assembly process of the artificial ommatidia layers in planar configuration. (*C*) Dicing of the assembled array in columns down to the flexible interconnection layer, which remains intact. (*D*) Curving of the ommatidial array along the bendable direction and attachment to a rigid semicylindrical substrate with a radius of curvature of 6.4 mm to build the CurvACE prototype. Two rigid circuit boards containing two microcontrollers, one three-axis accelerometer, and one three-axis rate gyroscope are inserted into the rigid substrate concavity and soldered to the sides of the ommatidia through dedicated pads (Figs. S3*D* and S4).

horizontal (Fig. 3*A*) and vertical (Fig. 3*D*) directions. The vertical interommatidial angles resulted in an average of $\Delta\varphi_v$ of 4.26° ± 0.16° (SD) (Fig. 3*D*), and the horizontal ones ranged from $\Delta\varphi_h$ = 4.2° ± 0.8° (SD) in the middle row (Fig. 3*A*) to 3.7° ± 0.7° (SD) in the top and bottom rows (Fig. 3*B*). The close match between the experimentally measured acceptance angles and interommatidial angles validates both the ray-tracing design and fabrication process while indicating that the CurvACE prototype, like the

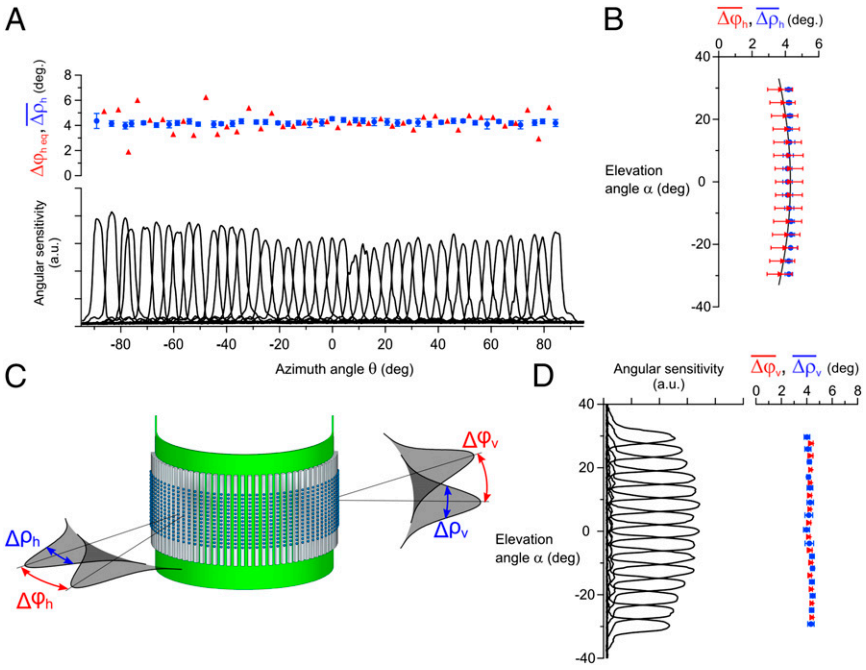

Fig. 3. Characterization of CurvACE angular sensitivity. (*A*) Measured ASF along the middle (equatorial) row (black curves), with the corresponding interommatidial angles $\Delta\varphi_{h\ eq}$ (red triangles) and mean acceptance angles $\Delta\rho_h$ (blue circles) of the CurvACE ommatidia averaged along every column. Error bars display SDs. (*B*) Mean horizontal interommatidial and acceptance angles averaged along every row of artificial ommatidia as a function of the elevation angle α. The black curve shows the theoretical $\Delta\varphi_h$ values obtained using Eq. S10 with a constant $\Delta\varphi_{h\ max}$ of 4.2°. (*C*) Schematic representation of the acceptance angle $\Delta\rho$ of an ommatidium and the interommatidial angle $\Delta\varphi$ calculated from the peak ASFs of two neighboring ommatidia. (*D*) Measured ASFs along a single column of artificial ommatidia (black curves), mean vertical interommatidial (red triangles), and acceptance angles (blue circles) averaged along every row of artificial ommatidia. a.u., arbitrary units; deg., degree.

fruit fly compound eye (24), performs an adequate sampling of its entire FOV (Fig. 1*B*). The observed spread in the values of the horizontal interommatidial angles $\Delta\varphi_h$ (Fig. 3 *A* and *B*) is probably due to the manual process used to mechanically fix the flexible PCB supporting the artificial ommatidia array onto the rigid curved substrate.

Characterization of Ommatidium Light Adaptation. In the natural world, visual sensors must cope with a wide dynamic range of irradiance, which can span on the order of 8 decades over the course of a day. Light variations within a scene are particularly challenging because they can make part of the visual field nonresponsive due to photoreceptor saturation. Animal retinae partly solve this crucial problem by means of a local light adaptation mechanism integrated within each photoreceptor (3, 4, 25, 26). Similarly, we have equipped each prototype ommatidium with a neuromorphic adaptation circuit (Fig. S2*D*) that operates independent of its 629 neighbors. The neuromorphic circuit originally proposed by Delbrück and Mead (27) was modified here by cascading a first-order, low-pass filter (Fig. S2*D*). This modification prevents temporal aliasing and keeps the photodetector bandwidth of 300 Hz practically constant across the entire studied range of ambient lighting conditions. The circuit design was further optimized (*SI Text, Photodetector Layer*) to minimize the transient gain dispersion of each autoadaptive circuit. Fig. 4 shows the mean steady state and transient responses of 11 artificial ommatidia (photodetectors with optics) in one column to light step increments and decrements presented at four different steady light levels (Fig. S6). At each of these four levels (red circles in Fig. 4), the output response of the individual ommatidia to light steps yields an S-shaped operating curve in a semilog plot. Adaptation to a novel steady irradiance level essentially produces a horizontal shift of the curve without markedly changing its slope, which represents a dynamic sensitivity of about 1,300 mV per decade in the linear part. The steady operating curve (shown in red in Fig. 4) is also a logarithmic function of the adapting light, but with a slope (steady sensitivity) about 12-fold smaller. Thanks to the optimized design of the adaptive photodetector layout, the averaged dispersion of the sensitivity over the four operating curves is as small as 11 mV, that is, only about 2% of the total 600-mV dynamic range.

The four operating curves demonstrate not only the high sensitivity of the prototype ommatidia but their relative invariance in sensitivity to the ambient light. These V(log I) curves shifting with the operating points are reminiscent of those obtained in analogous

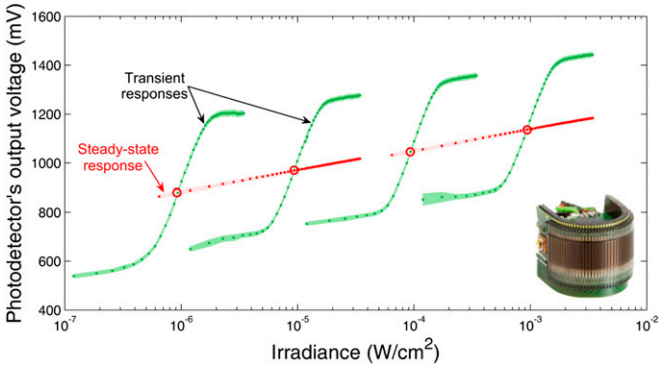

Fig. 4. CurvACE autoadaptation to ambient light at the single ommatidium level. Steady-state (red dots) and transient (green dots) responses of the adaptive analog VLSI photodetectors [design based on a circuit proposed by Delbrück and Mead (27)]. Each of the four dynamic operating curves (in green) shows the V(log I) response, averaged over 11 ommatidia (photodetectors with optics) of one column, to step increments and decrements of irradiance (Fig. S6) about four steady levels (red circles).

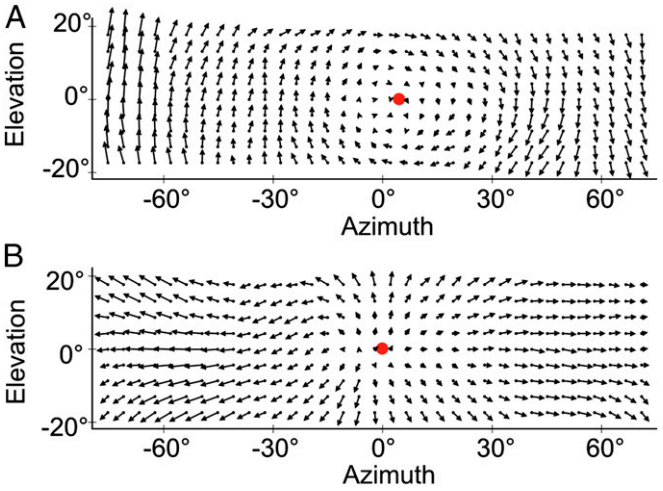

Fig. 5. Optic flow fields from the CurvACE prototype. Cylindrical equidistant projections of the optic flow field calculated with a modified version of the Lucas–Kanade method (29, 30) from the visual signals obtained by the CurvACE prototype subjected to roll motion (Fig. S8*B*) at 32° per second and at a distance of about 1 m to a wall displaying random black and white patterns (*A*) or to linear translation (Fig. S8*C*) at 3 cm/s toward the patterned wall at a distance of 1 cm (*B*). The red spot displays the center of rotation (*A*) or the focus of expansion (*B*).

experiments carried out on single vertebrate (25) and invertebrate (26) photoreceptors. This local adaptation is essential for efficient sampling of natural environments because it prevents saturation of the photoreceptors by bright spots in the visual scene while allowing them to adapt quickly to untoward illumination changes, such as transitions from a shaded area to a sunny place.

Characterization of Motion Extraction. In addition to an extensive FOV (Fig. 3) and local adaptation to illuminance (Fig. 4), the CurvACE prototype ommatidia yield a signal acquisition bandwidth of 300 Hz, which is threefold higher than that measured in the ommatidia of fast-flying insects (28). A high bandwidth contributes to the reduction of motion aliasing during fast locomotion. Furthermore, the implemented read-out protocol (Fig. S7) allows a maximum frame rate of 1.5 kfps, which permits frame averaging to improve the signal-to-noise ratio. We experimentally tested CurvACE motion detection capabilities by computing optic flow vectors from visual signals resulting from different types of motion in the presence of random black and white patterns on a wall (Fig. S8). In this first experiment, we used a modified version of the Lucas–Kanade method (29, 30) (*SI Text, Optic Flow Characterization* and Eqs. S1–S9), which is a particularly efficient image-based processing algorithm used to calculate optic flow vectors in two dimensions. The optic flow vectors measured during roll rotation (Fig. 5*A*) and linear translation toward a textured wall 0.3 s before collision (Fig. 5*B*) show coherent patterns of visual rotation and expansion, respectively. The center of rotation and focus of expansion can be clearly identified (red dots in Fig. 5), allowing for estimation of the axis of rotation and of the direction of translation, respectively. The sensor egomotion can be estimated from these flow fields, for instance, by implementing matched filters (31) analogous to the directionally selective, motion-sensitive neurons found in some insect visual systems (5). Furthermore, the embedded inertial sensors can be used for cancelling the rotational component of the measured optic flow, assessing only the translational component. Because this component is related to distance from objects, the optic flow data provided by a CurvACE prototype could assist mobile platforms to perform collision-free navigation (9).

We also characterized motion detection quantitatively at different ambient light levels with a bioinspired local visual processing

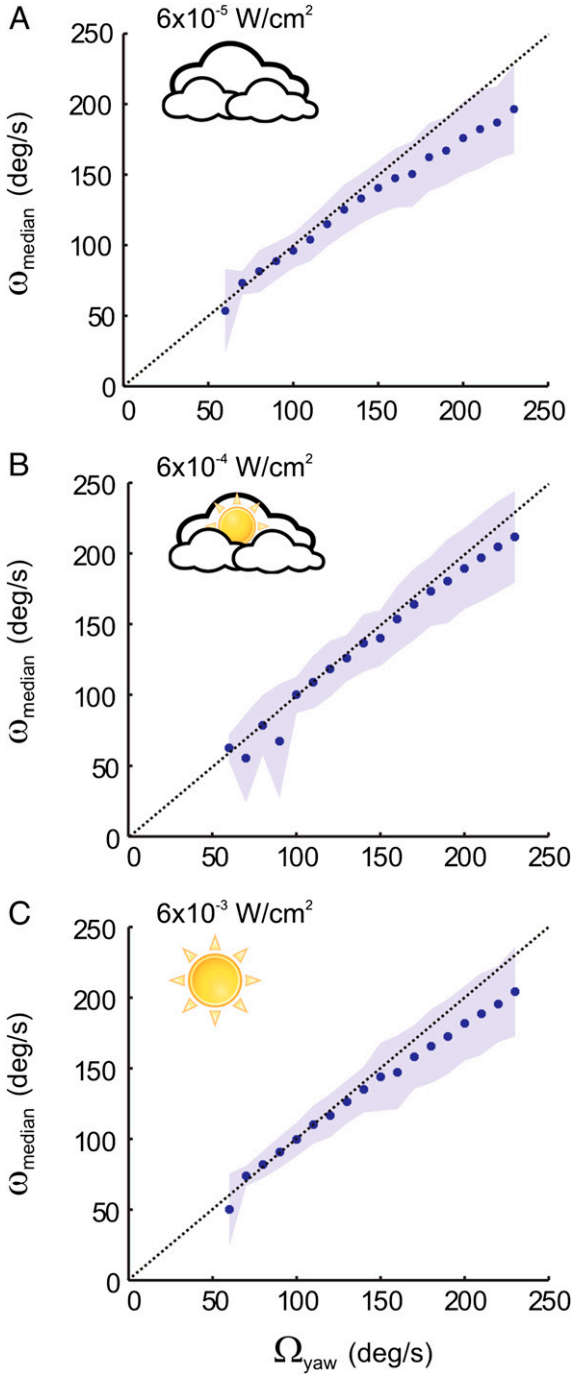

Fig. 6. Characterization of CurvACE motion detection capabilities. (*A–C*) Angular speed characteristics of CurvACE calculated with a method based on the time-of-travel scheme (32) (Fig. S9) assessed by applying steps of yaw rotational speed Ω_{yaw} to the sensor at 10° per second, lasting 10 s each, with the prototype placed at the center of a 105-cm diameter arena lined with prints of a natural image. The dashed line displays the theoretical trend.

algorithm based on the "time-of-travel" scheme (32) (Fig. S9). Fig. 6 shows the angular speed ω_{median} obtained by measuring the rotational optic flow as a function of the yaw rotational speed of CurvACE surrounded by a natural pattern. The experimental data show a good match between the rotational speed perceived by CurvACE and the true rotational speed. The error in the regression coefficient (linearity error) ranges from 5 to 10% (Fig. 6) at the three illumination levels, indicating that the CurvACE sensor takes full advantage of its autoadaptive analog VLSI photodetectors to make motion detection largely invariant to different illumination conditions. With the time-of-travel scheme, any pair of neighboring ommatidia driving a "local motion sensor" is able to measure angular velocities ranging from 50° to 358° per second for the interommatidial angle of 4.2° with sufficient accuracy. Measurement limitation at lower speeds is due to the signal attenuation brought about by the spatiotemporal processing present in each artificial ommatidium (Fig. S9*A*).

Discussion

The prototype presented here represents one of many possible manifestations of the CurvACE design principle. It yields a compact, lightweight, energy-efficient, miniature vision sensor that suits a broad range of applications requiring fast motion detection across a panoramic FOV. The applied optical and electronic parameters enable this prototype to measure optic flow patterns caused by sensor egomotion within a contrasted environment. A prototype with these characteristics could be used for autonomous terrestrial navigation, in analogy with some crab species (33) that use quasicylindrical compound eyes to navigate in flat environments. Furthermore, the hemispherical FOV of the prototype obtained by horizontal bending and by the longer microlens vertical pitch distance resembles the FOV of flying insects (1). Thus, such a prototype could also be used in Micro Air Vehicles (MAV) to support a large number of navigation tasks, such as egomotion estimation (34), collision avoidance (6, 7), and flight control (8, 9, 35), at low and high speeds, even in complex indoor and outdoor environments.

The CurvACE design principle also allows for flexible customization of artificial ommatidia in terms of their number, size, focal length, and interommatidial and acceptance angles, according to the requirements of the intended use. The artificial ommatidia could be further tailored by taking inspiration from the extraordinary eye regionalization found in insects and crustaceans, where specific parts of the compound eye serve specific functions. For example, higher acuity (36) may be obtained by increasing ommatidial resolution in defined areas, which could be achieved by decreasing both the acceptance angle and the interommatidial angle through redesigned microlenses and a reduced photodetector size with a consequent loss of signal-to-noise ratio. Design variations in the ommatidial optics or photodetector characteristics could yield regions of higher light capture (37) or different spectral (38) or polarization sensitivity (39).

The size of the CurvACE prototype described here is comparable to that of some trilobite eyes (22) (Fig. 1*C*) and some crab eyes (33), but reaching the diminutive size of insect eyes is challenging because it implies various tradeoffs. Increasing the surface density of artificial ommatidia requires decreasing photosensor size, chip circuitry, and microlens diameter at the cost of lower sensitivity and signal-to-noise ratio. Considering state-of-the-art technologies, we have estimated that the CurvACE prototype could be further reduced by a factor of 2. Further increments of surface density via hexagonal arrangement of ommatidia, similar to that found in many insect eyes, may be possible but would require different cutting methods. In the future, the development of vertical integration of 3D electronic circuits could further reduce the footprint size at the cost of chip thickness.

The CurvACE design opens up new avenues for vision sensors with alternative morphologies and FOVs of up to 360° in small, compact packages. In particular, the realization of a fully cylindrical CurvACE with a 360° FOV in the horizontal plane is relatively straightforward, either by attaching two semicylindrical prototypes (Fig. S4*D*) or by fabricating a wider array with a larger number of ommatidia. A CurvACE prototype with a truly omnidirectional FOV, reminiscent of the eye morphology of most

flying insects, would be especially interesting for egomotion estimation and better navigational support in three dimensions in a minimal package, providing an advantageous alternative to current cumbersome arrangements based on catadioptric or fish-eye lenses (9). A spherical CurvACE could be realized by fabricating and individually bending several ommatidial arrays with one ommatidium per column along the meridians of a sphere to measure optic flow omnidirectionally.

The CurvACE design is expected to foster further research and applications on fully flexible vision sensors (40, 41) that can adapt to rigid or unsteady surfaces of arbitrary shapes. Such devices could function as thin wearable sensors on smart clothing, as sensors for intelligent homes, or integrated in the artificial skin of soft robots. Toward these applications, future work could devise methods for cost-effective mass production of artificial ommatidia, which would also allow more complex dicing to achieve alternative bending patterns. Such production methods may include the realization of all processes of ommatidia alignment and assembly at the wafer level with the help of robotic platforms for automatized pick-and-place, bonding, and dicing.

ACKNOWLEDGMENTS. We thank Jean-Christophe Zufferey and Jacques Duparré for conceptual suggestions; Stéphanie Godiot, Patrick Breugnon, Alain Calzas, Rémy Potheau, and Marc Boyron for their help in VLSI circuit design and tests; Felix Kraze for assisting in prototype assembly; Julien Diperi for test bench realization; David O'Carroll and Russell Brinkworth for the natural photograph used in optic flow characterization setup; Antoine Beyeler for the CurvACE prototype photograph; and Claudio Bruschini for project management. We also thank the anonymous reviewers, whose comments have contributed largely to improve the manuscript. The CURVACE project acknowledges the financial support of the Future and Emerging Technologies (FET) program within the Seventh Framework Programme for Research of the European Commission, under FET-Open Grant 237940. This work also received financial support from the Swiss National Centre of Competence in Research Robotics of the Swiss National Science Foundation, the French National Center for Scientific Research and Aix-Marseille University, the French National Research Agency, and the German Federal Ministry of Education and Research.

1. Land MF, Nilsson D-E (2002) *Animal Eyes* (Oxford Univ Press, Oxford).
2. Kirschfeld K (1976) The resolution of lens and compound eyes. *Neural Principles in Vision*, eds Zettler F, Weiler R (Springer, Berlin), pp 354–370.
3. Laughlin SB (1989) The role of sensory adaptation in the retina. *J Exp Biol* 146(1): 39–62.
4. Gu Y, Oberwinkler J, Postma M, Hardie RC (2005) Mechanisms of light adaptation in Drosophila photoreceptors. *Curr Biol* 15(13):1228–1234.
5. Krapp HG, Hengstenberg R (1996) Estimation of self-motion by optic flow processing in single visual interneurons. *Nature* 384(6608):463–466.
6. Franceschini N, Pichon JM, Blanes C (1992) From insect vision to robot vision. *Philos Trans R Soc Lond B Biol Sci* 337(1281):283–294.
7. Blanchard M, Rind FC, Verschure PFMJ (2000) Collision avoidance using a model of the locust LGMD neuron. *Robot Auton Syst* 30(1–2):17–38.
8. Franceschini N, Ruffier F, Serres J (2007) A bio-inspired flying robot sheds light on insect piloting abilities. *Curr Biol* 17(4):329–335.
9. Floreano D, Zufferey J-C, Srinivasan MV, Ellington C (2009) *Flying Insects and Robots* (Springer, Berlin).
10. Duparré J, Dannberg P, Schreiber P, Bräuer A, Tünnermann A (2005) Thin compound-eye camera. *Appl Opt* 44(15):2949–2956.
11. Jeong K-H, Kim J, Lee LP (2006) Biologically inspired artificial compound eyes. *Science* 312(5773):557–561.
12. Radtke D, Duparré J, Zeitner UD, Tünnermann A (2007) Laser lithographic fabrication and characterization of a spherical artificial compound eye. *Opt Express* 15(6): 3067–3077.
13. Pulsifer DP, Lakhtakia A, Martín-Palma RJ, Pantano CG (2010) Mass fabrication technique for polymeric replicas of arrays of insect corneas. *Bioinspir Biomim* 5(3): 036001.
14. Qu P, et al. (2012) A simple route to fabricate artificial compound eye structures. *Opt Express* 20(5):5775–5782.
15. Khang D-Y, Jiang H, Huang Y, Rogers JA (2006) A stretchable form of single-crystal silicon for high-performance electronics on rubber substrates. *Science* 311(5758): 208–212.
16. Dinyari R, Rim S-B, Huang K, Catrysse PB, Peumans P (2008) Curving monolithic silicon for nonplanar focal plane array applications. *Appl Phys Lett* 92(9):091114–091113.
17. Xu X, Davanco M, Qi X, Forrest SR (2008) Direct transfer patterning on three dimensionally deformed surfaces at micrometer resolutions and its application to hemispherical focal plane detector arrays. *Org Electron* 9(6):1122–1127.
18. Lee J, Kim J (2011) Fabrication of strongly anchored, high aspect ratio elastomeric microwires for mechanical and optical applications. *J Micromech Microeng* 21(8): 085016–085024.
19. Jung I, et al. (2011) Dynamically tunable hemispherical electronic eye camera system with adjustable zoom capability. *Proc Natl Acad Sci USA* 108(5):1788–1793.
20. Dumas D, et al. (2012) Infrared camera based on a curved retina. *Opt Lett* 37(4): 653–655.
21. Ferrat P, et al. (2008) Ultra-miniature omni-directional camera for an autonomous flying micro-robot. *Conference on Optical and Digital Image Processing*, eds Schelkens P, Ebrahimi T, Cristobal G, Truchetet F (*Proc SPIE*, Bellingham, WA), Vol 7000, pp 70000M-1–70000M-10.
22. Fortey R, Chatterton B (2003) A Devonian trilobite with an eyeshade. *Science* 301(5640):1689.
23. Webb B (2002) Robots in invertebrate neuroscience. *Nature* 417(6886):359–363.
24. Götz KG (1965) Die optischen Übertragungseigenschaften der Komplexaugen von Drosophila. *Biol Cybern* 2(5):215–221, German.
25. Normann RA, Perlman I (1979) The effects of background illumination on the photoresponses of red and green cones. *J Physiol* 286(1):491–507.
26. Matić T, Laughlin SB (1981) Changes in the intensity-response function of an insect's photoreceptors due to light adaptation. *J Comp Physiol* 145(2):169–177.
27. Delbrück T, Mead CA (1994) Adaptive photoreceptor with wide dynamic range. *IEEE International Symposium on Circuits and Systems* (IEEE, New York, NY), pp 339–342.
28. Laughlin SB, Weckström M (1993) Fast and slow photoreceptors—A comparative study of the functional diversity of coding and conductances in the Diptera. *J Comp Physiol A Neuroethol Sens Neural Behav Physiol* 172(5):593–609.
29. Lucas BD, Kanade T (1981) An iterative image registration technique with an application to stereo vision. *Proceedings of the Seventh International Joint Conference on Artificial Intelligence*, ed Hayes PJ (William Kaufmann, Los Altos, CA), pp 674–679.
30. Fleet DJ, Langley K (1995) Recursive filters for optical flow. *IEEE Trans Pattern Anal Mach Intell* 17(1):61–67.
31. Franz MO, Krapp HG (2000) Wide-field, motion-sensitive neurons and matched filters for optic flow fields. *Biol Cybern* 83(3):185–197.
32. Pichon J-M, Blanes C, Franceschini N (1989) Visual guidance of a mobile robot equipped with a network of self-motion sensors. *Mobile Robots IV*, eds Chun WH, Wolfe WJ (*Proc SPIE*, Vol 1195), pp 44–55.
33. Zeil J, Al-Mutairi M (1996) The variation of resolution and of ommatidial dimensions in the compound eyes of the fiddler crab Uca lactea annulipes (Ocypodidae, Brachyura, Decapoda). *J Exp Biol* 199(Pt 7):1569–1577.
34. Plett J, Bahl A, Buss M, Kühnlenz K, Borst A (2012) Bio-inspired visual ego-rotation sensor for MAVs. *Biol Cybern* 106(1):51–63.
35. Kerhuel L, Viollet S, Franceschini N (2010) Steering by gazing: An efficient biomimetic control strategy for visually guided micro aerial vehicles. *IEEE Trans Robot* 26(2): 307–319.
36. Horridge GA (1978) The separation of visual axes in apposition compound eyes. *Philos Trans R Soc Lond B Biol Sci* 285(1003):1–59.
37. Hateren JH, Hardie RC, Rudolph A, Laughlin SB, Stavenga DG (1989) The bright zone, a specialized dorsal eye region in the male blowfly Chrysomyia megacephala. *J Comp Physiol A Neuroethol Sens Neural Behav Physiol* 164(3):297–308.
38. Franceschini N, Hardie R, Ribi W, Kirschfeld K (1981) Sexual dimorphism in a photoreceptor. *Nature* 291(5812):241–244.
39. Labhart T (1980) Specialized photoreceptors at the dorsal rim of the honeybee's compound eye: Polarizational and angular sensitivity. *J Comp Physiol* 141(1):19–30.
40. Daneshpanah M, Javidi B (2011) Three-dimensional imaging with detector arrays on arbitrarily shaped surfaces. *Opt Lett* 36(5):600–602.
41. Dobrzynski MK, Pericet-Camara R, Floreano D (2012) Vision Tape—A flexible compound vision sensor for motion detection and proximity estimation. *IEEE Sens J* 12(5): 1131–1139.
42. Franceschini N, Kirschfeld K (1971) Les phénomènes de pseudopupille dans l'œil composé de Drosophila. *Biol Cybern* 9(5):159–182. French.
43. Heisenberg M, Wolf R (1984) *Vision in Drosophila: Genetics of Microbehavior* (Springer, Berlin).
44. Lee JH, et al. (2010) Sestrin as a feedback inhibitor of TOR that prevents age-related pathologies. *Science* 327(5970):1223–1228.

Supporting Information

Floreano et al. 10.1073/pnas.1219068110

SI Text

Prototype Parts and Assembly

Optics Layer. The generation of the compound eye multiaperture optics involves the formation of a chirped microlens array (lenslet diameter of 172 μm) and two chirped aperture arrays (1) (Fig. S1*C*). This implies toroidal-shaped lenslets and pitch differences between the layers and the photodetectors on the sensor wafer as well (microlens pitch of 290 μm > photoreceptor pitch of 260 μm). The microlenses are formed by reflow of photoresist and subsequent UV molding of a highly transparent polymer (Ormocer, Ormocomp; Micro Resist Technology) (Fig. S1 *A* and *B*). Low-reflective chromium films are used to create two aperture layers, which are deposited by sputtering and patterned by UV photolithography and subsequent metal etching. The optics f-number is 2.4. The resist patterning and UV molding have been carried out using a mask aligner device (Süss Microtec AG).

Photodetector Layer. This layer consists of an optoelectronic chip fabricated in silicon at wafer level using CMOS technology (0.35-μm technology with Opto option; X-FAB Semiconductor Foundries). Every chip has a size of 20×6.765 mm^2 and consists of 42 columns, each bearing 15 VLSI autoadaptive photodetectors, a bias circuit, a 10-bit analog-to-digital converter (ADC), and a logic circuit that implements a serial interface for the read-out protocol (Fig. S2).

Every autoadaptive photoreceptor consists of a logarithmic circuit associated with a high-gain negative feedback loop as proposed by Delbrück and Mead (2) (Fig. S2*D*). A MOSFET transistor (M_{FB} in Fig. S2*D*) operates in the subthreshold region where the current-to-voltage characteristic follows a logarithmic law. Thus, the photoreceptor operates over several decades of ambient light level, generating the low-gain direct current operating curve shown as a red dotted line in Fig. 4. In addition, transient signals are amplified with a variable gain depending on the equivalent resistance of the adaptive element: The lower the output signal level (V_{out}), the higher is the gain. The autoadaptive feature is used to compensate for ambient light changes, that is, to keep the photodetectors responding to contrasting features even in intense ambient lighting. The overall bandwidth of the photoreceptor depends on the current (I_{ph} in Fig. S2*D*) flowing into the photodiode and on the time constants of the amplifier stage. For high ambient lighting levels, the bandwidth can be as large as 500 kHz. To prevent aliasing during the digitization process, we deliberately enhanced the circuit by limiting the bandwidth of each photodetector to about 300 Hz by cascading it with an antialiasing filter, consisting of a first-order low-pass filter based on a transconductance amplifier. To limit the dispersion due to the CMOS technology, we finely adjusted the ratio between the two capacitors (C_1 and C_2 in Fig. S2*D*) to minimize the transient gain dispersion of the photodetectors.

Every photoreceptor column bears a multiplexer and a 10-bit ADC with a conversion time of 15 μs. The analog signal of the 15 photodetectors is sequentially converted by the multiplexed ADC and sent to the microcontroller unit through a synchronous serial interface.

Printed Circuit Boards. ***Interconnection layer.*** Printed circuit boards (PCBs) are used to connect the different electronic components of the curved artificial compound eye (CurvACE) electrically while ensuring their mechanical support. In the case of the ommatidia interconnection layer, a polyimide (Kapton) one-layer PCB with a thickness of 100 μm is used. The low thickness and the absence of vias allow curving the ommatidia down to the required 6.4-mm radius of curvature (ROC). The middle part of the PCB is left empty of tracks because that is the position where the photoreceptor layer is placed. Tracks for analog and digital power and ground, as well as for clock, sync, and digital data read-out, are routed to operate all columns (read-out protocol is shown in Fig. S7).

Rigid internal PCBs. The CurvACE prototype bears two rigid PCBs that, in addition to the interconnection layer of the artificial ommatidia, provide mechanical and electrical support to the internal electronic components. They are made of FR-4 (fiberglass with epoxy resin), have a nominal thickness of 0.5 mm, and are placed in the concavity of the sensor and perpendicular to the flex PCB. They are electrically connected to the artificial ommatidia by connecting pads placed along their edges (Fig. S4). Both rigid PCBs are also interconnected electrically via those connecting pads through tracks designed along the outer side of the interconnection layer.

The used electronic components of the CurvACE prototype are soldered onto these rigid PCBs. More precisely, the microcontrollers of model dsPIC33FJ128GP802 (Microchip Technology) are soldered on top of each PCB. Two inertial sensors, a three-axis accelerometer MMA7455L (Freescale Semiconductor), and a three-axis rate gyroscope ITG-3200 (InvenSense) are placed at the bottom side of the top PCB. Two low-drop-out voltage regulators EXAR-SP6201EM5-L-3-3 (EXAR) and the external connector lie at the bottom side of the bottom PCB (Fig. S3).

Ommatidia Assembly Process. ***Bonding.*** The alignment and glue bonding assembly of the three artificial ommatidia layers is done via a Fineplacer device (Finetech GmbH & Co. KG, Berlin, Germany) that yields a precision down to 1 μm. The glue bonding between the optics and photoreceptor layers is realized with a high-transparent UV-curing adhesive EPO-TEK OG 146 (Epoxy Technology Inc., Billerica, MA). To improve the bonding strength, a silane-based adhesion promoter has been applied to both surfaces before gluing. The glue bonding between the photoreceptor and the interconnection layer is realized applying a thermally curing adhesive EPO-TEK 353ND. The photoreceptor layer is electrically connected with the interconnection layer by wedge bonding with aluminum wires of 30 μm. The wires are protected with a transparent glob-top material (Fig. S3*A*).

Intercolumn dicing. The dicing of the bonded optics and photoreceptor layer in 42 columns is realized by an automatic dicing setup (DISCO Corp.). A special 100-μm-thick synthetic-resin compound dicing blade for rigorous and brittle materials was applied for trenching and dicing the columns.

Prototype Assembly. A rigid and hard internal scaffold fabricated in polyoxomethylene by five-axis milling with CNC technology is used as mechanical support of the CurvACE PCBs.

For the prototype assembly, the artificial ommatidia supported by the flex PCB are bent and placed onto the curved outer side of the scaffold, which bears the required ROC of 6.4 mm, and are subsequently fixed. The rigid PCBs, bearing the microcontrollers and inertial sensors soldered (Fig. S4), are introduced in the cylinder concavity along two mechanical guides in the scaffold. Subsequently, the rigid PCB side pads are soldered to the ommatidia flex PCB end pads.

Read-Out Interface. The CurvACE prototype uses a serial direct connection protocol as a read-out interface to communicate with the controller units (Fig. S7). It consists of a unique clock signal sent to each ommatidial column, two sync signals used to start

the ADC conversion of the associated columns, and a digital signal per column used for the serial transfer of each ommatidium output signal. The clock and sync signals are emitted by the embedded microcontrollers, which also collect the output data for processing. With a clock frequency of 1 MHz and an ADC conversion time of 16 μs for each ommatidium, the maximum frame rate that can be achieved is 1.95 kfps. After protocol implementation, the measured frame rate for this prototype is 1.5 kfps.

Characterization Setups

Ommatidia Sensitivity Characterization. ***Optical characterization.*** The optical characterization of the CurvACE prototype implies the characterization of the optical angular sensitivity of each pixel in both directions: along rows and along columns (Fig. 3 *A* and *D*). For this, a LabVIEW software suite [including Real-Time and Field-Programmable Gate Array (FPGA) LabVIEW software; National Instruments] was used to acquire data from the CurvACE prototype through a 16-bit serial peripheral interface (SPI) bus. To characterize the angular sensitivity of each pixel, the CurvACE prototype is set on a test bench (Fig. S5) composed of two rotary stages to select a specific row or column, two linear stages (2 df and 3 df) to set the center of rotation accurately at the center of the CurvACE prototype, a stepper motor to rotate the cylindrical CurvACE by steps of 0.1° along a specific row or column, and a resolver to measure accurately the actual prototype rotation imposed by the stepper motor. The angular position is then calculated by the FPGA software at 4 kHz. A goniometer supporting the overall mechanical assembly performs the line or column selection with a resolution of 1 arc minute (0.017°). To change the configuration of the test bench between row and column characterization, the setup is readapted. In particular, adjustments of the 3-df linear stages are made with metrology instruments.

A 20-Hz flickering point light source based on a white light emitting diode (LED), followed by a diaphragm with a diameter of 1 mm, is placed at a distance of 2.8 m from the photodetectors to illuminate them from a predetermined direction. Stepper motor control, angular measurements, and signal acquisition from the CurvACE are achieved through a LabVIEW NI Embedded Software Evaluation Toolkit (National Instruments). The obtained signal, which represents the ommatidia ASF shown in Fig. 3 *A* and *D*, has been smoothed by means of a low-pass filter.

Light sensitivity characterization. We developed a programmable light box able to create an illuminance varying between 1 and 10,000 lux at a distance of 3 cm, where the CurvACE prototype was placed. The light intensity could be digitally adjusted through an RS232 bus. This highly controlled light environment allows the response of an ommatidium (photodetector with optics) to be measured both as a function of the steady illuminance and as a function of incremental and decremental light steps presented about the steady illuminance (Fig. S6). Very low illuminance values were obtained by means of an additional neutral density glass filter (thickness of 2 mm, optical density OD = 2, HG3; Schott) placed between the LED (TLWR7600; Vishay) and the *CurvACE* prototype. An additional digital input signal sent by the FPGA software was used to synchronize the changes in light intensity with the CurvACE readout. The irradiance of the light source was measured by means of a radiometer (ILT1700, International Light Technologies Inc., Peabody, MA), whose probe was placed at a distance of 28 mm from the light source.

Optic Flow Characterization. Optic flow was extracted from the CurvACE sensor by subjecting it to different kinds of motion while acquiring the photoreceptor signals on a personal computer. For this, the sensor was mounted at the tip of a mechanical arm, allowing for its free positioning and orientation (Fig. S8*A*). Two different setups are used. To impose a rotational motion, the prototype sensor is mounted on a rotary table surrounded by patterned cardboard. The rotary disk is driven by a stepper motor at a fixed rotational speed between 4.5° and 40° per second (Fig. S8*B*). For imposing a translational motion, the sensor is mounted on a carriage driven by a stepper motor via a tension chain. Fig. S8*C* shows the carriage on rails passing by a textured wall. For the flow pattern shown in Fig. 5*B*, the sensor was frontally approaching a wall showing the same texture.

For the experiments in translation, and roll rotation (Fig. 5), we used a noniterative, gradient-based, multiframe optic flow extraction method derived from the one developed by Lucas and Kanade (3) and inspired by the work of Fleet and Langley (4). Before computation, a bias in the response of the CurvACE ommatidia is removed to improve gradient calculation. The algorithm is derived from the optic flow constraint

$$I_x u + I_y v + I_t = 0, \qquad \textbf{[S1]}$$

which can be derived from the image brightness constancy assumption using first-order Taylor expansion. Here, (u, v) is the flow vector and I is the image function, with subscripts denoting partial derivatives. A spatiotemporal weighted least-squares solution at time t over the image patch P is given by

$$min \sum_{i=0}^{\infty} \sum_{x,y \in P} w(i)\big(I_x(x,y,t-i)u + I_y(x,y,t-i)v + I_t\big(x,y,t-i\big)\big)^2 = 0, \qquad \textbf{[S2]}$$

with $w(i) = (1-\alpha)\alpha^i$ defining the exponential weighting function in the time domain. This can be solved by

$$(u, v) = G^{-1}A, \qquad \textbf{[S3]}$$

$$G(t) = \sum_{i=0}^{\infty} w(i)G'\big(t-i\big), \qquad \textbf{[S4]}$$

$$A(t) = \sum_{i=0}^{\infty} w(i)A'\big(t-i\big), \qquad \textbf{[S5]}$$

$$G'(t) = \sum_{P} \nabla I \nabla I^T, \qquad \textbf{[S6]}$$

$$A'(t) = \sum_{P} I_t \nabla I, \qquad \textbf{[S7]}$$

which leads to the iterative solution

$$G(t) = \alpha G(t-1) + (1-\alpha)G'(t), \qquad \textbf{[S8]}$$

$$A(t) = \alpha A(t-1) + (1-\alpha)G'(t). \qquad \textbf{[S9]}$$

Using a temporal filter scheme allows one to use a smaller integration window. The temporal filter value α was set to 0.96. The size of the integration window for the results shown is a 5×5 ommatidia patch. For the gradient computation, we use the kernel $[-1,0,1]$. Thus, we require a single additional ommatidium at each border of the 5×5 integration window for optic flow computation, getting a total of 45 ommatidia. The size of the integration window and the gradient kernel limits the area for flow computation, because we wanted to avoid special cases at the border. With the given parameters, we have a border of three ommatidia where no optic flow can be computed.

For the experiments aimed at assessing CurvACE ability to extract optic flow in various light environments (Fig. 6), we used an optic flow extraction method based on a time-of-travel scheme (5). Photoreceptor signals are acquired from the equatorial row of ommatidia (Fig. S9*C*). Any two neighboring ommatidia drive a local motion sensor (LMS). The two spatially low-pass-filtered photodetector signals are temporally band-pass-filtered, and a hysteresis threshold is then set on each channel to determine the time Δt elapsed between their excitations. The local angular speed ω_i is then obtained simply via a look-up table, which calculates the ratio between the interommatidial angle $\Delta\varphi_i$ and the time lag Δt_i (Fig. S9*A*). Following the results obtained on fly motion-sensing neurons (6, 7), the LMS is actually split into two parallel and independent channels dealing each with either the "ON" or "OFF" component of the moving contrast (Fig. S9*B*). Furthermore, each pair of adjacent ommatidia actually drives two LMSs of opposite directions (+/−) that process ω^+_i and ω^-_i, respectively. Because the angular speed of contrasting features moving in the preferred direction is always higher than that measured in the nonpreferred direction, the magnitude of the optic flow vector ω_{median} is measured from the maximum between the median value ω^+_{median} and ω^-_{median} of all possible LMS outputs in the equatorial row.

Eq. S10.

$$\Delta\varphi_h = \mathrm{acos}\left(1+\cos^2(\alpha)\left(\cos(\Delta\varphi_{h\ max})-1\right)\right) \qquad \textbf{[S10]}$$

Due to the hemispherical field of view of the CurvACE sensor (Fig. 1*B*), the horizontal interommatidial angle $\Delta\varphi_h$ gradually decays with the elevation angle α (Fig. 3*B*) according to Eq. **S10**, with $\Delta\varphi_{h\ max}$ being the interommatidial angle at the equator ($\Delta\varphi_{h\ max}$= 4.2° in our prototype) and α ranging from −30° to 30° in our prototype.

1. Duparré J, Dannberg P, Schreiber P, Bräuer A, Tünnermann A (2005) Thin compound-eye camera. *Appl Opt* 44(15):2949–2956.
2. Delbrück T, Mead CA (1994) Adaptive photoreceptor with wide dynamic range. *IEEE International Symposium on Circuits and Systems,* pp 339–342.
3. Lucas BD, Kanade T (1981) An iterative image registration technique with an application to stereo vision. *Proceedings of the Seventh International Joint Conference on Artificial Intelligence*, ed Hayes PJ (William Kaufmann, Los Altos, CA), pp 674–679.
4. Fleet DJ, Langley K (1995) Recursive filters for optical flow. *IEEE Trans Pattern Anal Mach Intell* 17(1):61–67.
5. Pichon J-M, Blanes C, Franceschini N (1989) Visual guidance of a mobile robot equipped with a network of self-motion sensors. *Mobile Robots IV*, eds Chun WH, Wolfe WJ (*Proc SPIE*, Vol 1195), pp 44–55.
6. Franceschini N, Riehle A, Le Nestour A (1989) Directionally selective motion detection by insect neurons. *Facets of Vision*, eds Stavenga DG, Hardie RC (Springer, Berlin), pp 360–390.
7. Eichner H, Joesch M, Schnell B, Reiff DF, Borst A (2011) Internal structure of the fly elementary motion detector. *Neuron* 70(6):1155–1164.

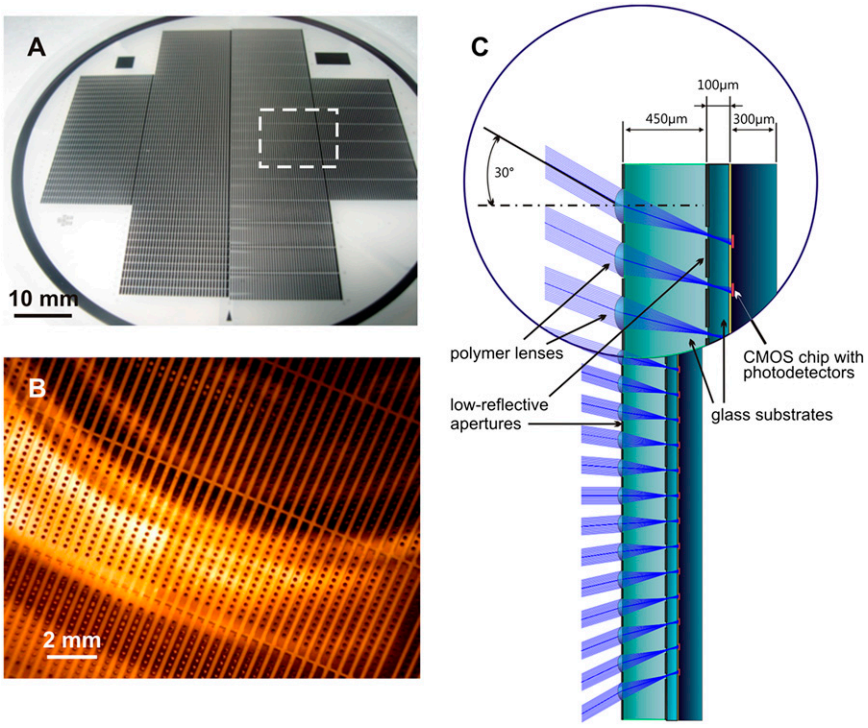

Fig. S1. Fabrication and design of the compound eye optics. (*A*) Image of the full-processed optical wafer (AF32; Schott) carrying arrays of aperture patterns and microlenses. Those destined for the presented CurvACE prototypes are placed at the right half of the wafer. (*B*) Detail of the array wafer area shown in *A* with a white dashed square. (*C*) Cross-section through an ommatidial column and ray tracing (Zemax; Radiant Zemax, LLC) in the optics layer. The blue rays show the path of the light focused by each microlens on its photoreceptor (red) via two apertures.

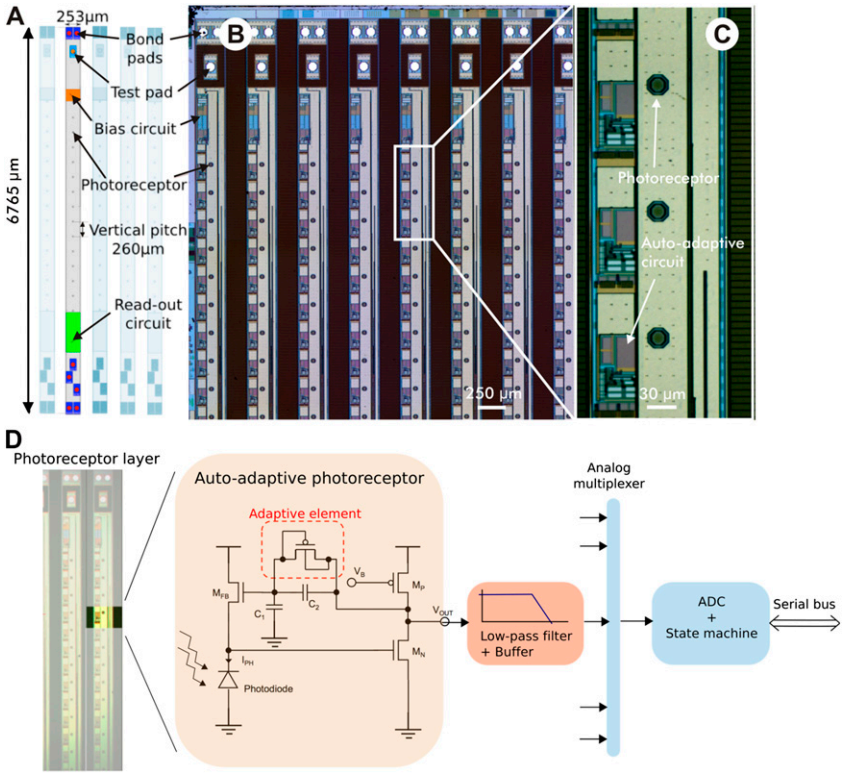

Fig. S2. Layout of the photoreceptor layer. (*A*) Schematic layout of a column of the photoreceptor layer. (*B*) High-definition image of the top part of the columns of the photoreceptor layer. (*C*) Detail of three octagonal-shaped photodetectors each connected to an adaptive analog VLSI circuit. (*D*) Basic layout of the photoreceptor processing and read-out architecture implemented within each column of the CurvACE ommatidia. The original circuit proposed by Delbrück and Mead (2) was enhanced here by cascading a first-order low-pass filter to prevent temporal aliasing.

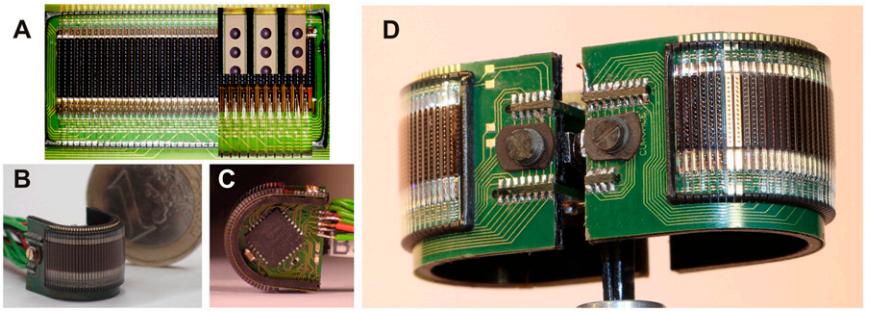

Fig. S3. CurvACE ommatidia and prototype assembly. (*A*) Image of the planar ommatidial array just after assembly and column dicing. (*Right Inset*) Details of the microlens array surface, as well as the wire bonding between the photoreceptor and the interconnection layers, are shown. Perspective image of the CurvACE prototype (*B*), top view (*C*), and configured to provide a 360° field of view (FOV) (*D*).

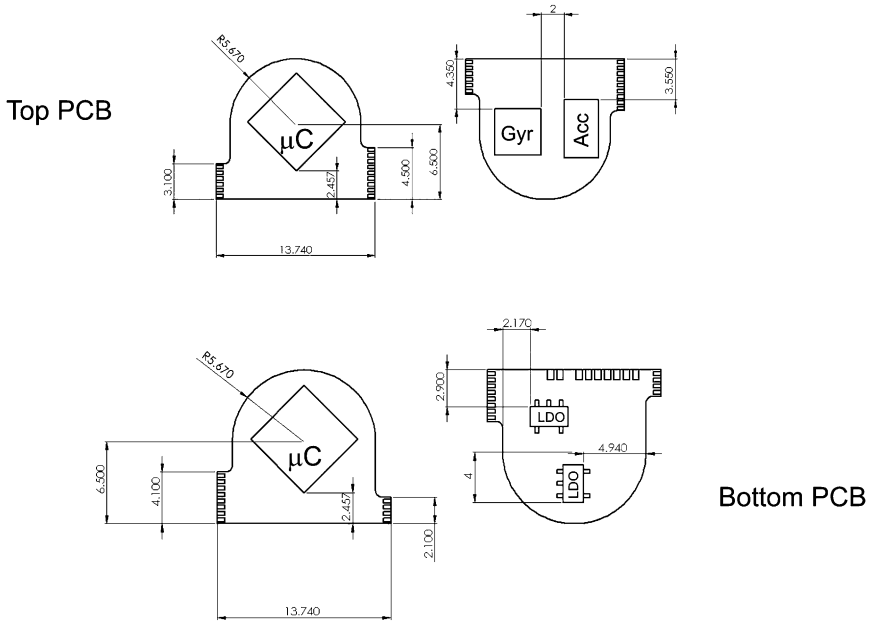

Fig. S4. Scheme of the two rigid PCBs showing their electronic components assembled. Acc, accelerometer; μC, for microcontroller; Gyr, rate gyroscope; LDO, low-drop-out voltage regulator. The top side (*Left*) and bottom side (*Right*) of the PCB are displayed. The dimensions are in millimeters.

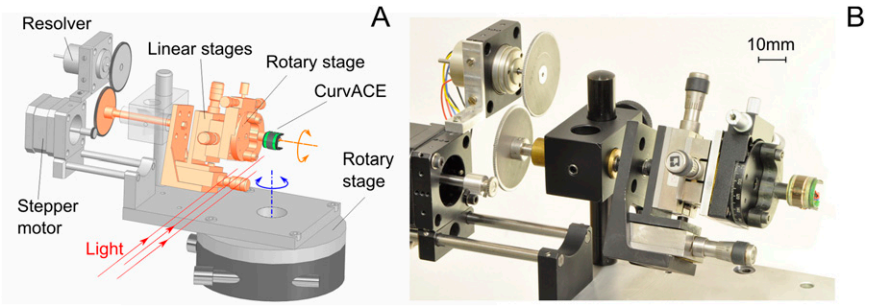

Fig. S5. Setup for the measurement of the angular sensitivity function (ASF) of CurvACE ommatidia. (*A*) Computer-aided design (CAD) of the characterization bench configured for characterizing the horizontal ASF of a row of ommatidia placed in front of a point light source. The stepper motor rotates the sensor slowly about the horizontal axis (double circular orange arrow), whereas the resolver measures the actual angular position with a resolution of 0.08°. To select the row to be characterized, a second rotary stage (double circular blue arrow) allows the CurvACE to be oriented accurately with respect to the point light source. (*B*) Photograph of the CurvACE mounted at the tip of the characterization setup.

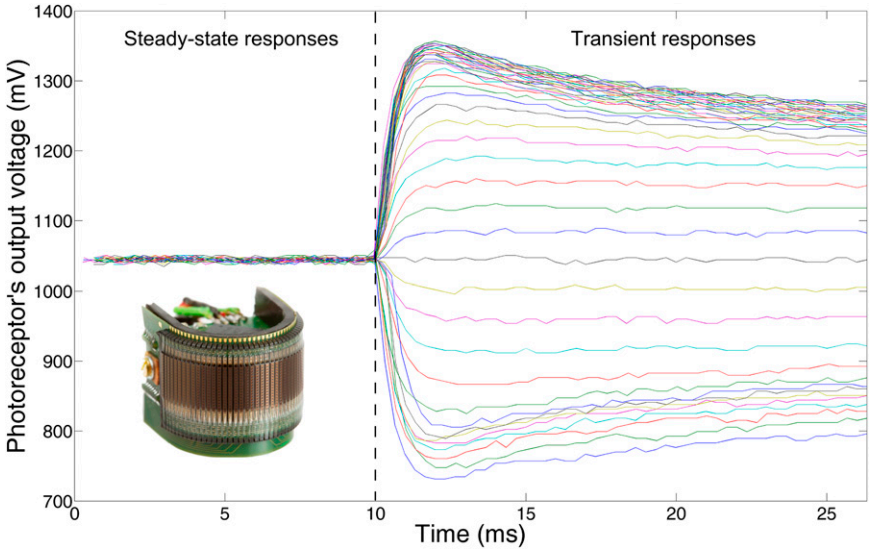

Fig. S6. Step responses of a single artificial ommatidium (photodetector with optics) in response to incremental and decremental light steps (51 steps) applied at $t = 10$ ms (vertical dotted line). The ommatidium output signal was digitized at a sampling frequency of 3 kHz. The steady-state value (red circles in Fig. 4) was acquired 20 s after the steps were applied. Each of the four dynamic operating curves (green points in Fig. 4) plots the peak amplitude of the step responses of the ommatidium output signal as a function of log I.

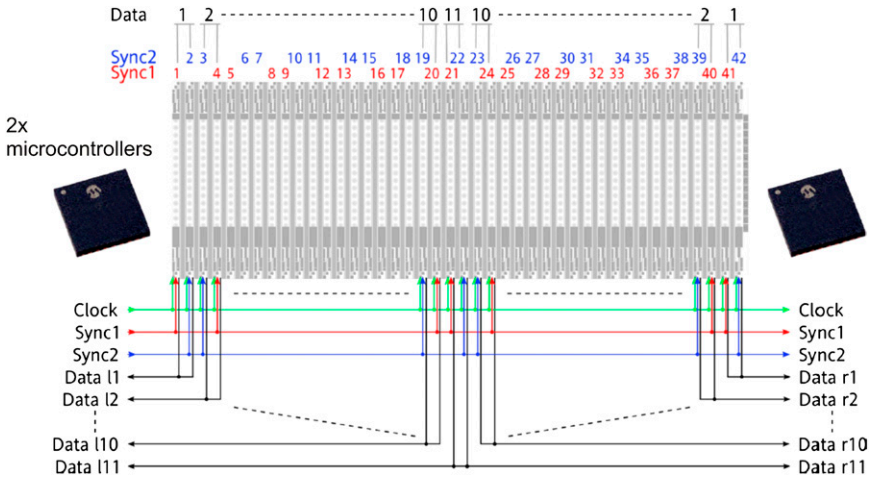

Fig. S7. Read-out protocol of CurvACE prototype. Scheme of the read-out interface in the prototype. "Clock" represents the clock signal sent to each ommatidial column. "Sync 1 and 2" are the two sync signals used to start the ADC conversion of the associated columns (red and blue columns associated with Sync 1 and 2 signals, respectively). "Data 1–11" are the digital signals used for the serial transfer of each ommatidium output signal.

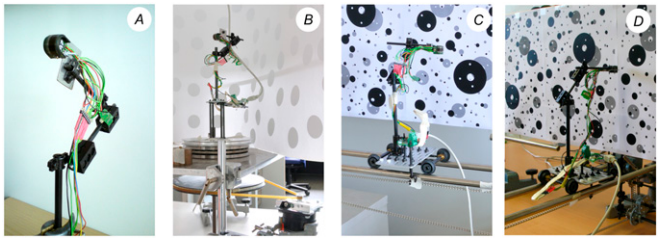

Fig. S8. Setup for the rotation and translation experiments. (*A*) Mechanical arm holding the CurvACE sensor. (*B*) Motor-driven rotary table used for testing the ability of the CurvACE to extract rotational optic flow. Motor-driven carriage to test the ability of the CurvACE to extract panoramic translational optic flow along a corridor (*C*) and toward a wall (*D*).

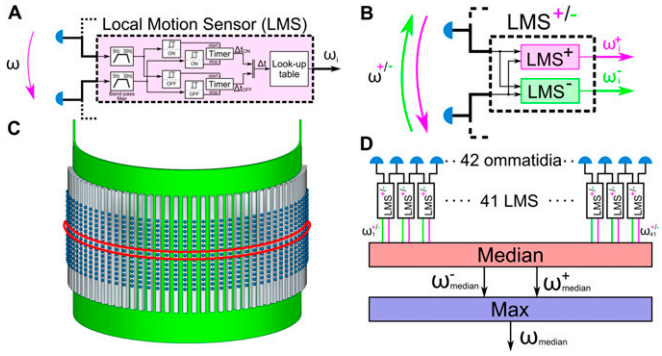

Fig. S9. Visual motion measurement along one dimension. (*A*) General processing architecture of an LMS driven by two adjacent ommatidia and taking into account both ON and OFF contrast transitions. (*B*) Scheme of angular speeds observed by the LMS in opposite directions. (*C*) Scheme highlighting the central row of ommatidia in the CurvACE prototype, where the visual signals for yaw motion computation were extracted (Fig. 6). (*D*) Scheme of the statistical calculation of the observed angular speed. Max, maximum.